CONTENTS

Supplementary Note 1. CONSTRUCTION OF EFFECTIVE TIGHT-BINDING HAMILTONIAN FROM CIRCUIT LATTICE

In this section, we provide the theoretical correspondence between the effective tight-binding Hamiltonian in Eq. (1) in the main text and the designed circuit Laplacian in Eq. (4).

A. Sample fabrication details

We fabricated a circuit with 8×8 lattice on a printed circuit board. In x-direction, we implemented two capacitors $C_a = 47$ nF and $C_b = 94$ nF in parallel with controllable switch between each node to achieve effective intracell coupling C_1 and intercell coupling C_2. By adjusting the toggle switches, three different capacitances can be obtained in a single lattice as, C_a, C_b, and $C_a + C_b$ respectively. This configuration allows in-situ observation of topological phase transition for different boundary conditions by adjusting both bulk and boundary hopping elements. The anisotropic coupling along y-direction is realized by The negative impedance converters through current inversion (INIC), which is composed of operational amplifier with capacitors $C_3 = 47$ nF, $C_4 = 94$ nF and inductors $L_1 = 150$ μH, $L_2 = 75$ μH.

B. Effective tight-binding model

Our proposed setup adopts a square lattice of the two-dimensional electrical circuit network, which consists of two sublattice sites per unit cell. The tight-binding Hamiltonian of the lattice model can be expressed as,

$$H = \sum_{x,y} (v-w)\hat{a}^\dagger_{x,y+1}\hat{a}_{x,y} + (v+w)\hat{a}^\dagger_{x,y}\hat{a}_{x,y+1} - (v+w)\hat{b}^\dagger_{x,y+1}\hat{b}_{x,y} - (v-w)\hat{b}^\dagger_{x,y}\hat{b}_{x,y+1} \\ + t_1(\hat{b}^\dagger_{x,y}\hat{a}_{x,y} + \hat{a}^\dagger_{x,y}\hat{b}_{x,y}) + t_2(\hat{a}^\dagger_{x+1,y}\hat{b}_{x,y} + \hat{b}^\dagger_{x,y}\hat{a}_{x+1,y}), \tag{1}$$

where t_1, t_2 represent the intracell and intercell coupling strength, $v \pm w$ denotes asymmetric coupling strength. The operator $\hat{a}^\dagger_{x,y}(\hat{b}^\dagger_{x,y})$ and $\hat{a}_{x,y}(\hat{b}_{x,y})$ are the creation and annihilation operators on the site $a(b)$. The corresponding tight-binding Hamiltonian in momentum space can be represented by 2×2 matrix form as,

$$H(k) = \begin{bmatrix} (v+w)e^{-ik_y} + (v-w)e^{ik_y} & t_1 + t_2 e^{ik_x} \\ t_1 + t_2 e^{-ik_x} & -(v+w)e^{ik_y} - (v-w)e^{-ik_y} \end{bmatrix}. \tag{2}$$

By using Pauli matrices representation, we can rewrite the Hamiltonian as,

$$H(k) = (-2iw \sin k_y)I + (2v \cos k_y)\sigma_z + (t_1 + t_2 \cos k_x)\sigma_x + (-t_2 \sin k_x)\sigma_y. \tag{3}$$

C. Derivation of circuit Laplacian

Our circuit model is designed to realize the tight-binding Hamiltonian in Eq. (3). Kirchhoff's rule dictates the relations between current and voltage of each site, and it can be represented in the frequency domain as,

$$I(\omega) = J(\omega)V(\omega), \tag{4}$$

where $\omega = 2\pi f$ is AC driving frequency. $I(\omega)$ is the matrix of input current. $V(\omega)$ is the matrix of the measured voltage and circuit Laplacian $J(\omega)$ is an admittance matrix that takes the role of tight binding Hamiltonian.

We now derive the expression of the circuit Laplacian, $J(\omega)$, for our system. We apply Kirchhoff's laws to each side of the designed model shown in Fig. S1**a**. We obtain the explicit equations of the current flows as,

$$\begin{aligned} I_1 + I_2 &= I_3 + I_2 e^{-ik_y} + G_a, \\ I_3 + I_4 &= I_1 e^{-ik_x} + I_4 e^{-ik_y} + G_b, \end{aligned} \tag{5}$$

where $I_i (i = 1, 2, 3, 4)$ denote the current flows at each node and G_a, G_b represent the grounding part at node a, b. Note that an additional grounding part is adopted to eliminate the diagonal terms of open circuit Laplacian at the

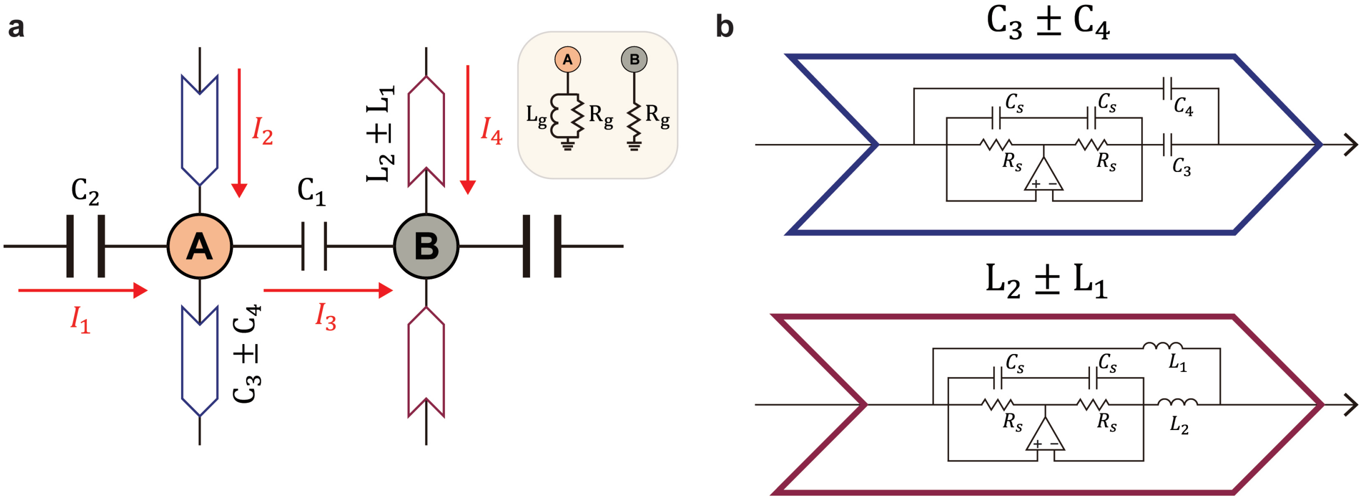

Supplementary Figure 1. Layout of unit cell of circuit and INIC a Schematic of a unit cell of circuit. Red arrows denote the direction of current labeled $I_i (i = 1, 2, 3, 4)$. Inset shows node A and B grounded by inductor L_g and resistor R_g for A, and resistor R_g for B. **b** Illustration of detail structure of INICs. Blue (red) is composed of operational amplifier with capacitors (inductors). Arrow shows the direction of strong capacitive (inductive) coupling $C_3 + C_4$ $(L_1 + L_2)$ while opposite direction of coupling is $C_3 - C_4$ $(L_1 - L_2)$.

resonance frequency, which ensures the pure imaginary identity matrix. By plugging in the detailed information of the circuit components, we derive the explicit expression between the current and voltage in each node as,

$$
\begin{aligned}
I_a = i\omega^{-1}[&-\omega^2 V_a^{x,y} + \omega^2 C_1 (V_b^{x-1,y} - V_a^{x,y}) + \omega^2 C_2 (V_b^{x,y} - V_a^{x,y}) \\
&+\omega^2 (C_3 - C_4)(V_a^{x,y+1} - V_a^{x,y}) + \omega^2 (C_3 + C_4)(V_1^{x,y-1} - V_a^{x,y})], \\
I_b = i\omega^{-1}[&-\omega^2 V_b^{x,y} + \omega^2 C_2 (V_a^{x,y} - V_b^{x,y}) + \omega^2 C_1 (V_a^{x+1,y} - V_b^{x,y}) \\
&-(\frac{1}{L_1} + \frac{1}{L_2})(V_b^{x,y+1} - V_b^{x,y}) - (\frac{1}{L_1} - \frac{1}{L_2})(V_b^{x,y-1} - V_b^{x,y}),
\end{aligned}
\tag{6}
$$

where the superscripts, (x, y), represent the coordinates of the unit cell and V_a, V_b denotes the voltage at node a, b respectively. By applying Fourier transformation to Eq. (6), we finally derive the matrix form of the circuit Laplacian in momentum space, which is given as,

$$
J(\mathbf{k}, \omega) = i\omega \begin{bmatrix} C_1 + C_2 + 2C_3 - 2C_3 \cos k_y - 2iC_4 \sin k_y - \frac{1}{\omega^2 L_g} & -C_1 - C_2 e^{-ik_x} \\ -C_1 - C_2 e^{ik_x} & C_1 + C_2 - \frac{2}{\omega^2 L_1} + \frac{1}{\omega^2 L_1} 2\cos k_y - \frac{1}{\omega^2 L_2} 2i \sin k_y \end{bmatrix},
\tag{7}
$$

Again, C_1 is the effective intracell coupling capacitance between nodes a,b, and C_2 is the effective intercell coupling capacitance between adjacent unit cells in the x-direction. The capacitances C_3, C_4 and inductances L_1, L_2 are employed for anisotropic coupling in y-direction. The grounded inductance $L_g = \frac{1}{4} L_1$ at node a is adopted to guarantee the same resonance condition of unit cell. In order to ensure the resonance condition at all nodes and obtain the equivalent coupling strength in the opposite direction, we set the capacitance-inductance relation as $C_1 + C_2 = 2C_3$, $L_1 C_3 = L_2 C_4$. At the resonance condition, the circuit Laplacian is rewritten in terms of the Pauli matrices representation as,

$$
(i\omega_0)^{-1} J(\mathbf{k}, \omega_0) = (-2iC_4 \sin k_y)\mathrm{I}_2 + (-2C_3 \cos k_y)\sigma_z + (C_1 + C_2 \cos k_x)\sigma_x + (-C_2 \sin k_x)\sigma_y,
\tag{8}
$$

where $\omega_0 = 1/\sqrt{L_1 C_3} = 1/\sqrt{L_2 C_4}$ denotes the resonance frequency of LC resonator.

Finally, we equate the general tight-binding model Hamiltonian in Eq. (3) and circuit Laplacian as,

$$
v = -C_3, \quad w = C_4, \quad t_1 = C_1, \quad t_2 = C_2,
\tag{9}
$$

where the sign of capacitance is determined by the direction of current in Kirchhoff's law.

Supplementary Note 2. THEORETICAL DETAILS ON TOPOLOGICAL INVARIANT

In this section, we provide the theoretical details on the definition of the topological invariants.

A. Correspondence of the circuit model with Kawabata-Sato-Shiozaki model

We show the correspondence of our system with the Kawabata-Sato-Shiozaki(KSS) model[1]. We rewrite the Hamiltonian of our model in Eq. (3) as,

$$H(k_x, k_y) = -(2iw \sin k_y)I + (t_1 + t_2 \cos k_x)\sigma_x + (-t_2 \sin k_x)\sigma_y + (2v \cos k_y)\sigma_z. \tag{10}$$

In the limit $2v = 2w = t_2 = \lambda$ and the transformation, $k_x \to -k_x$, $k_y \to -k_y + \frac{\pi}{2}$, $\sigma_x \leftrightarrow \sigma_y$, the Hamiltonian reduces as,

$$H(k_x, k_y) = -i\lambda \cos k_y I + (\lambda \sin k_x)\sigma_x + (t_1 + \lambda \cos k_x)\sigma_y + (\lambda \sin k_y)\sigma_z, \tag{11}$$

which is equal to the Hamiltonian of the KSS model up to a constant term in the identity matrix. As a result our original model in Eq. (10) also preserves the reminiscent of the non-Hermitian C_4 symmetry up to a constant shift, which is given as,

$$-i\sigma_x H^\dagger(k_x, k_y + \frac{\pi}{2}) = H(-k_y, k_x + \frac{\pi}{2}). \tag{12}$$

In Ref. [1], it is shown that the presence of this C_4 rotational symmetry is crucial for the topological protection of the second-order non-Hermitian skin effect. Here, we note that the emergence of the skin state in our system does not rely on this symmetry, and it is stabilized in general values of coupling strengths.

B. Calculation of the Hopf invariant

In this section, we provide the detailed method of calculating the Hopf invariant (also known as the three-dimensional winding number). We consider the deformation of the Hamiltonian in Eq. (10) as a function of the dimerization along the x-direction and the non-reciprocity along the y-direction. To do so, we introduce the auxiliary periodic parameter, $\phi \in [0, 2\pi)$ and the extended Hamiltonian as a function of the momentum and t. The extended Hamiltonian, $H_{\mathrm{ex}}(k, \phi)$ is defined on the three-dimensional torus T^3 ($(k_x, k_y, \phi) \in T^3$).

$$H_{\mathrm{ex}}(\mathbf{k}, \phi) = if_0(\mathbf{k}, \phi)\mathrm{I}_2 + f_x(\mathbf{k}, \phi)\sigma_x + f_y(\mathbf{k}, \phi)\sigma_y + f_z(\mathbf{k}, \phi)\sigma_z. \tag{13}$$

The specific adiabatic deformation is considered with the following condition.

$$\begin{aligned} H_{\mathrm{ex}}(\mathbf{k}, \phi = 0) &= H_0(\mathbf{k})_{|t_2|>|t_1|, w>0}, \\ H_{\mathrm{ex}}(\mathbf{k}, \phi = \pi/2) &= H_0(\mathbf{k})_{|t_2|<|t_1|, w>0}, \\ H_{\mathrm{ex}}(\mathbf{k}, \phi = \pi) &= H_0(\mathbf{k})_{|t_2|<|t_1|, w=0}, \\ H_{\mathrm{ex}}(\mathbf{k}, \phi = 3\pi/2) &= H_0(\mathbf{k})_{|t_2|>|t_1|, w=0}, \end{aligned} \tag{14}$$

In the main text, we call the above Hamiltonians, second-order topological, first-order non-reciprocal, trivial atomic limit, first-order dimerized respectively. Since the extended Hamiltonian is a mapping from $T^3 \to S^3$, we can define the topological winding number, which is given as,

$$\mathcal{W} = \frac{1}{2\pi^2} \int_{S^3} \epsilon^{ijkl} \bar{f}_i d\bar{f}_j d\bar{f}_k d\bar{f}_l. \tag{15}$$

Mathematically. the winding number counts the surface area of S^3, which $\bar{f}(\mathbf{k}, t)$ covers.

In the main text, we used the following extended Hamiltonian to generate the Hopf bundle,

$$H_{\mathrm{ex}}(\mathbf{k}, \phi) = A(\phi)H_0(\mathbf{k})_{|t_2|>|t_1|, w>0} + B(\phi)H_0(\mathbf{k})_{|t_2|<|t_1|, w>0} + C(\phi)H_0(\mathbf{k})_{|t_2|<|t_1|, w=0} + D(\phi)H_0(\mathbf{k})_{|t_2|>|t_1|, w=0} \tag{16}$$

where $A(\phi), B(\phi), C(\phi), D(\phi)$ is explicitly chosen as (Fig. S2),

$$A(\phi) = exp(-\alpha\phi^2), \tag{17}$$
$$B(\phi) = exp(-\alpha(\phi - \pi/2)^2), \tag{18}$$
$$C(\phi) = exp(-\alpha(\phi - \pi)^2). \tag{19}$$
$$D(\phi) = exp(-\alpha(\phi - 3\pi/2)^2). \tag{20}$$

The above choice of the deformation protocol satisfies the condition Eq. (14).

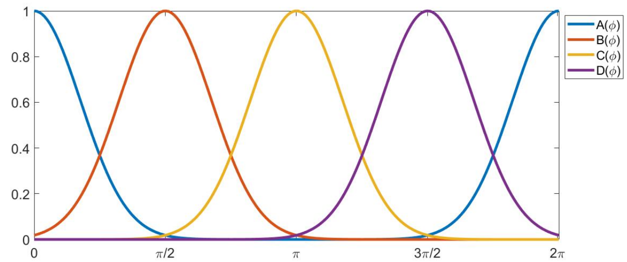

Supplementary Figure 2. Protocol of the adiabatic deformation, $A(\phi)$,$B(\phi)$,$C(\phi)$, $D(\phi)$.

C. Correspondence of three-dimensional winding number and Hopf invariant

In this section, we now establish the equivalence of the three-dimensional winding number of the circuit Hamiltonian and the Hopf invariant of the SSs for the non-Hermitian circuit Laplacian. In the main text, the Hamiltonian is given as,

$$H(\mathbf{k},\omega) = if_0(\mathbf{k},\omega)\mathrm{I}_2 + f_x(\mathbf{k},\omega)\sigma_x + f_y(\mathbf{k},\omega)\sigma_y + f_z(\mathbf{k},\omega)\sigma_z, \tag{21}$$

where $f_0 = -(\gamma + \lambda\cos k_x)$, $f_x = \lambda\sin k_y$, $f_y = \gamma + \lambda\cos k_y$, $f_z = \lambda\sin k_x$. From the KSS Hamiltonian, we perform singular-value decomposed as, $H_{\mathrm{T}}(\mathbf{k},\omega) = U^\dagger_{\mathbf{k}} D_{\mathbf{k}} V_{\mathbf{k}}$, to define the unitary matrix, $q_{\mathbf{k}} \equiv U^\dagger_{\mathbf{k}} V_{\mathbf{k}} \in U(2)$. In our specific model, we derive as,

$$q_{\mathbf{k}} = i\bar{f}_0(\mathbf{k},\omega)\mathrm{I}_2 + \bar{f}_x(\mathbf{k},\omega)\sigma_x + \bar{f}_y(\mathbf{k},\omega)\sigma_y + \bar{f}_z(\mathbf{k},\omega)\sigma_z \tag{22}$$

where $\bar{f}_i = f_i/\sqrt{|f_0|^2 + |f_x|^2 + |f_y|^2 + |f_z|^2}$. We now note that the vector of each coefficient lives on the three-dimensional sphere. i.e. $\{\bar{f}_0, \bar{f}_x, \bar{f}_y, \bar{f}_z\} \in S^3$

Since the third homotopy group of U(2) is non-trivial ($\pi_3(U(2)) = \mathbb{Z}$), we can define the three-dimensional winding number by introducing auxiliary time dimension as,

$$\mathcal{W} = \frac{1}{24\pi^2}\int_0^1 dt \int d^2\mathbf{k}\epsilon^{ijk}\mathrm{Tr}[q^\dagger_{\mathbf{k}}\partial_i q_{\mathbf{k}} q^\dagger_{\mathbf{k}}\partial_j q_{\mathbf{k}} q^\dagger_{\mathbf{k}}\partial_k q_{\mathbf{k}}]. \tag{23}$$

We now plug in the expression in (22) into (23). Using the relation, $q^\dagger_{\mathbf{k}}\partial_i q_{\mathbf{k}} = -(\partial_i q^\dagger_{\mathbf{k}})q_{\mathbf{k}}$ and $qq^\dagger = q^\dagger q = \mathrm{I}_2$, we can simplify the expression of the winding number is given as,

$$\begin{aligned}
&\epsilon^{ijk}\mathrm{Tr}[q^\dagger_{\mathbf{k}}\partial_i q_{\mathbf{k}} q^\dagger_{\mathbf{k}}\partial_j q_{\mathbf{k}} q^\dagger_{\mathbf{k}}\partial_k q_{\mathbf{k}}] \\
&= \epsilon^{ijk}\mathrm{Tr}[q_{\mathbf{k}}\partial_i q^\dagger_{\mathbf{k}}\partial_j q_{\mathbf{k}}\partial_k q^\dagger_{\mathbf{k}}] \\
&= \sum_{\alpha\beta\gamma\delta=1,2,3,4} \epsilon^{ijk}\bar{f}_\alpha\partial_i\bar{f}^*_\beta\partial_j\bar{f}_\gamma\partial_k\bar{f}^*_\delta \times \mathrm{Tr}[\sigma_\alpha\sigma_\beta\sigma_\gamma\sigma_\delta] \\
&= \sum_{\alpha\beta\gamma\delta=1,2,3,4} -2i\epsilon^{ijk}\epsilon^{\alpha\beta\gamma\delta}\bar{f}_\alpha\partial_i\bar{f}_\beta\partial_j\bar{f}_\gamma\partial_k\bar{f}_\delta
\end{aligned} \tag{24}$$

Finally, we arrive at the expression of the three-dimensional winding number in the main text (up to a sign difference), which is given as,

$$\mathcal{W} = -\frac{1}{2\pi^2}\int_{\partial\Omega}\epsilon_{\alpha\beta\gamma\delta}\bar{f}_\alpha d\bar{f}_\beta d\bar{f}_\gamma d\bar{f}_\delta, \tag{25}$$

where the integration is performed on the 3-sphere, $\bar{f} \in \partial\Omega = S^3$. We now consider the mapping of $\bar{f}$ to the pseudospin basis, which is given as,

$$m_i(\mathbf{k}) = z^\dagger(\mathbf{k})\sigma_i z(\mathbf{k}), \quad i = 1,2,3, \tag{26}$$

where $z(\mathbf{k}) = (\bar{f}_0 + i\bar{f}_x, \bar{f}_y + i\bar{f}_z)$ is the two-component pesudospinor. In this case, $\mathcal{W}$ corresponds to the Hopf invariant. [2, 3]

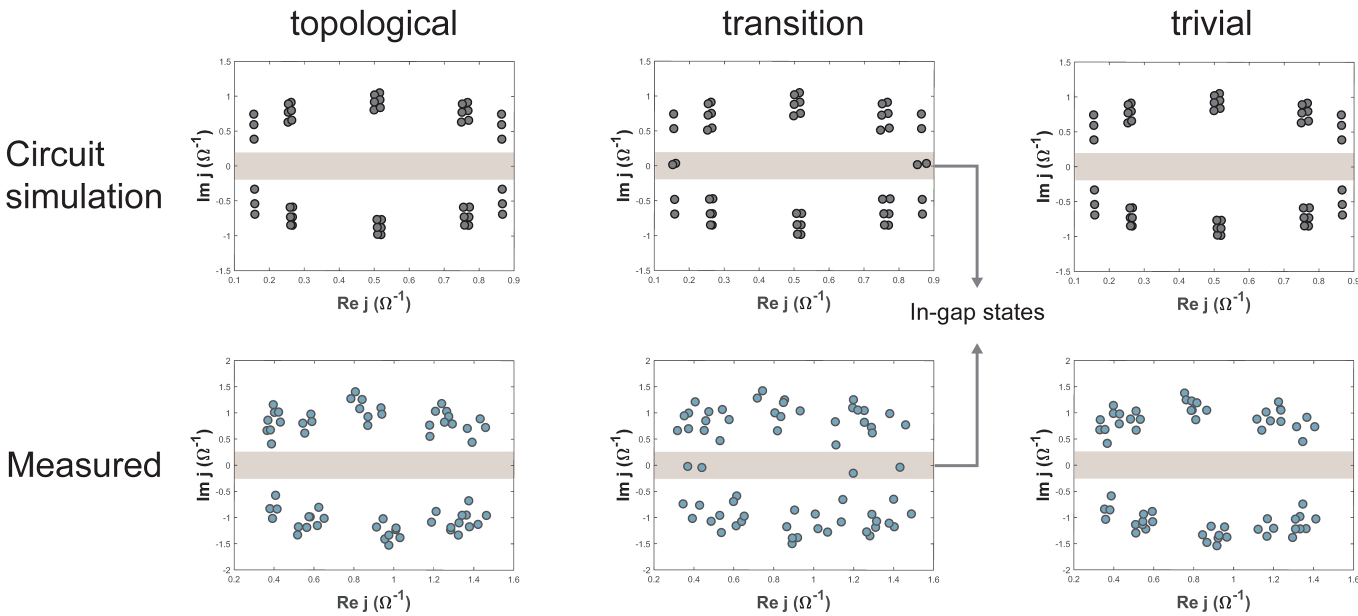

Supplementary Figure 3. Complex admittance spectra for periodic boundary condition (PBC) The direct comparison for theoretically simulated and experimentally obtained complex admittance spectrum for PBC in topological, transition, and trivial phase respectively. In the topological phase transition, the line gap closing is observed at Im j = 0 for both simulation and experimental data.

Supplementary Note 3. SPECTRAL ANALYSIS FOR PBC

We provide a detailed analysis of the complex admittance spectrum in PBC. In contrast to the complex admittance spectrum under OBC, the line gap is closed in PBC when the phase of matter is at the transition[1]. As discussed in the main text, the topological phase of our system is determined by the difference between intracell and intercell coupling which can be adjusted by utilizing the controllable switch in the circuit. We then measured three distinct phases of circuit Laplacian by manipulating the switch and obtained the corresponding complex admittance band spectrum. Fig. S3 shows the experimentally obtained and corresponding theory complex admittance band spectrum for topological, transition, and trivial phases respectively. The line gap is denoted as a gray region in the band spectrum. In the topological and trivial phase, the bulk band is separated by the line gap. At a phase transition, line gap closing occurs which can be identified by the in-gap states. As predicted in the theoretical result, our experimental data at a transition explicitly shows the in-gap states which are clear evidence for gapless phase transition. In the OBC counterpart, the corner-skin states manifest when the phase of the system is changed from trivial to topological phase (i.e., gapless phase transition) as shown in the main text Fig.4. Finally, by comparing PBC and OBC, we clearly confirm the gapless phase transition.

Supplementary Note 4. ASYMMETRIC COMPLEX ADMITTANCE SPECTRUM DUE TO PARASITIC EFFECTS.

In this section, we clarify the physical origin of the asymmetric complex admittance spectrum observed in the main text Fig.4. In the theoretical model of the main text, we assume that the magnitude of non-reciprocal coupling strength is equal for +y and -y directions. To explain the discrepancy between the theory and the experiment, we now consider the capacitive and inductive couplings of the INIC component for +y and -y directions separately as,

$$\begin{aligned} C_{+y} &= C_3 + C_4, \quad C_{-y} = C_3 - C_4, \\ L_{+y} &= L_1 - L_2, \quad L_{-y} = L_1 + L_2, \end{aligned} \tag{27}$$

where C_3, C_4, L_1, L_2 denote the capacitances and inductances of the operational amplifier in anisotropic direction respectively, as shown in the main text Fig. 1**d**. We now introduce disorder on capacitive and inductive coupling for

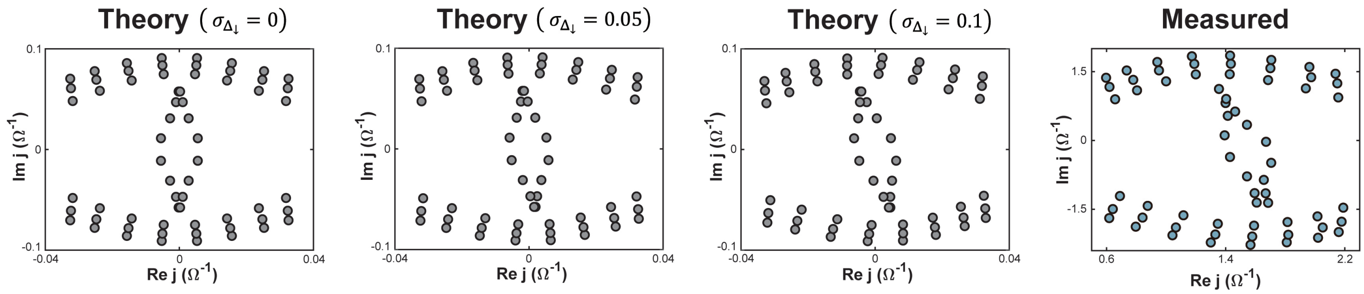

Supplementary Figure 4. Parasitic effect on anisotropic direction The calculated complex admittance band spectra for three distinct values of disorder (i.e., $\sigma_{\Delta_\downarrow} = 0$, $\sigma_{\Delta_\downarrow} = 0.05$, and $\sigma_{\Delta_\downarrow} = 0.1$) and experimentally obtained complex admittance band spectrum. We find that the addtion of the parasitic effect well-explains the observed asymmetric complex admittance spectrum.

down direction as

$$\begin{aligned} \delta C_{-y} &= C_{-y}(1+\sigma_{\Delta_\downarrow}) \\ \delta L_{-y} &= L_{-y}(1+\sigma_{\Delta_\downarrow}) \end{aligned} \tag{28}$$

where $\sigma_{\Delta_\downarrow}$ is the disorder value caused by the parasitic effect of capacitance and inductance for the down direction. The Fig. S4 shows the corrected theoretical calculations of the complex admittance band spectrum with the implementation of the disorder effect. It can be seen that the asymmetry of the complex admittance band spectrum is increased with the magnitude of the parasitic effect. When $\sigma_{\Delta_\downarrow} = 0.1$, the theoretical calculation well-explains the observed anisotropy in the experiment. As a result, we conclude that the anisotropy in our experimental data is caused by the parasitic effect of the capacitive and inductive coupling on the anisotropic direction. Furthermore, we explicitly confirmed the parasitic effect causes an asymmetric eigenvoltage distribution of corner-skin state as shown in Fig. S5 (No. 25, 26, 38, 39, 40 states).

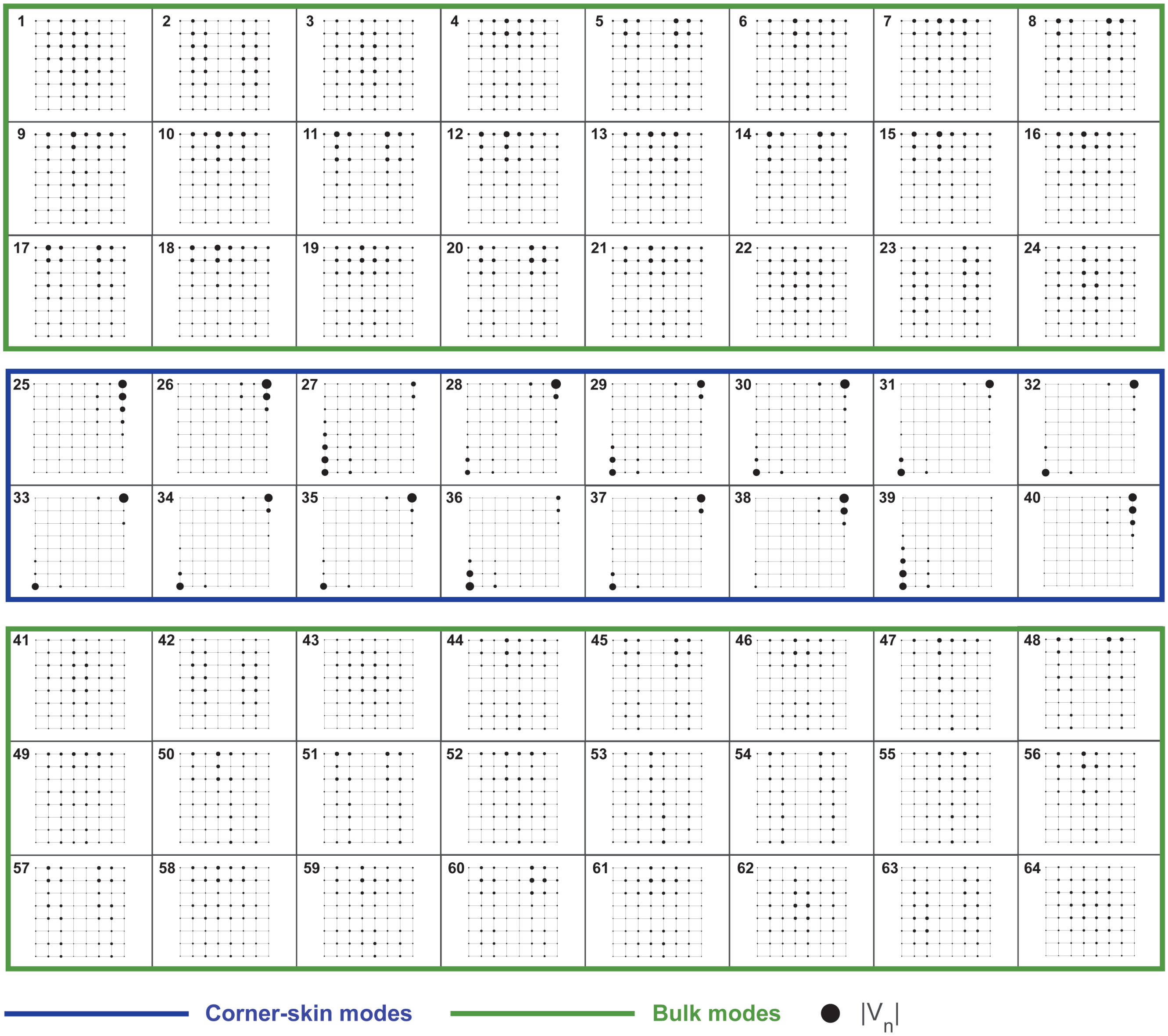

Supplementary Figure 5. All 64 voltage eigenstate distribution The voltage distribution of all eigenstates is plotted. The amplitude of voltage $|V_n|$ is weighted by the size of circle. In 8×8 lattice, the number of corner-skin states is 16 while the number of bulk states is 48. The voltage distributions in green box (i.e., No. $1 - 24, 41 - 64$) and blue box (i.e., No. $25 - 40$) represent the delocalized bulk states and corner-skin states, respectively. As discussed in Supplementary Material D, the asymmetric voltage distribution is observed due to the parasitic effect.

Supplementary References

[1] K. Kawabata, M. Sato, and K. Shiozaki, Higher-order non-hermitian skin effect, Phys. Rev. B **102**, 205118 (2020).

[2] J.-r. Ren, R. Li, and Y.-s. Duan, Inner topological structure of hopf invariant, Journal of Mathematical Physics **48**, 073502 (2007), https://doi.org/10.1063/1.2747614.

[3] R. Bott, L. W. Tu, *et al.*, *Differential forms in algebraic topology*, Vol. 82 (Springer, 1982).